

A rotating cavity for high-eld angle-dependent microwave spectroscopy of low-dimensional conductors and magnets

Susumu Takahashi and Stephen Hill

Department of Physics, University of Florida, Gainesville, FL 32611, USA

(Dated: March 23, 2024)

The cavity perturbation technique is an extremely powerful method for measuring the electrodynamic response of a material in the millimeter- and sub-millimeter spectral range (10 GHz to 1 THz), particularly in the case of high-eld/frequency magnetic resonance spectroscopy. However, the application of such techniques within the limited space of a high-eld magnet presents significant technical challenges. We describe a 7.62 mm \times 7.62 mm (diameter \times length) rotating cylindrical cavity which overcomes these problems. The cylinder is mounted transverse to the bore of the magnet, coupling is achieved through the side walls of the cavity, and the end plate is then rotated (by means of an external drive) instead of the body of the cavity itself. Therefore, rotation does not affect the cylindrical geometry, or the mechanical connections to the incoming waveguides. The TE₀₁₁ mode frequency of the loaded cavity is 51.863 GHz, with the possibility to work on higher-order modes to frequencies of order 350 GHz. Neither the quality factor ($Q \approx 22,000$ for the fundamental mode) or the coupling to the cavity are significantly affected for full 360° of rotation. The rotation mechanism provides excellent angle resolution ($< 0.1^\circ$), and is compact enough to enable measurements in the high-eld (up to 45 T) magnets at the National High Magnetic Field Laboratory. Two-axis rotation capabilities are also possible in conjunction with split-pair magnet configurations. We present examples of angle-dependent measurements which illustrate the unique capabilities of this rotating cavity, including: high-eld angle-dependent measurements of a novel form of cyclotron resonance in anisotropic organic conductors; and angle-dependent high-frequency single-crystal electron paramagnetic resonance (EPR) measurements in single-molecule magnets.

I. INTRODUCTION

In recent years, microwave (millimeter and sub-millimeter wave) technologies, covering frequencies from 10 GHz to 10 THz ($0.33 - 330 \text{ cm}^{-1}$), have become the focus of intensive efforts in many fields of research. In engineering and medicine, THz imaging represents one of the next-generation technologies, enabling non-destructive materials inspection, chemical composition analysis [1, 2, 3], and medical diagnoses [1, 2, 4]. In the fundamental sciences, physics, chemistry and biology, microwave spectroscopy is also very useful for investigating the physical properties of a material. This is particularly true for the sub-eld of condensed matter physics, where the millimeter and sub-millimeter spectral range can provide extremely rich information concerning the basic electronic characteristics of a material [5, 6, 7, 8]. Furthermore, combining microwave techniques and high magnetic elds (microwave magnetooptics), allows many more possibilities, including: cyclotron resonance (CR) [9, 10, 11, 12, 13, 14, 15, 16]; electron paramagnetic resonance (EPR) [17, 18, 19, 20]; antiferromagnetic resonance (AFMR) [21]; Josephson Plasma Resonance (JPR) measurements of layered superconductors [22, 23, 24, 25]; and many others. In each of these examples, the magnetic eld influences the dynamics of electrons at frequencies spanning the microwave spectral range. Another very important aspect of microwave magnetooptical investigations is the possibility to study angle dependent effects by controlling the angle between the sample and the microwave and DC electromagnetic elds. For instance, through stud-

ies of the angle dependence of CR amplitudes, one can extract detailed information concerning the Fermi surface (FS) topology of a conductor [15, 16]. Consequently, angle-dependent microwave spectroscopy has been widely used in recent years to study highly anisotropic magnetic and conducting materials. Problems which have been addressed using these methods include: high- T_c superconductivity [22], and other low-dimensional superconductors, e.g. organic conductors [11, 12, 13, 15, 16, 24, 25], Sr_2RuO_4 [14], etc.; the quantum and fractional quantum Hall effects [26, 27]; and low-dimensional magnets, including single-molecule magnets (SMMs) [18, 19, 20].

Unfortunately, the microwave spectral range presents many technical challenges, particularly when trying to study very tiny ($\sim 1 \text{ mm}^3$) single-crystal samples within the restricted space inside the bore of a large high-eld magnet system (either resistive or superconducting [28]). Problems associated with the propagation system stem from standing waves and/or losses [29]. Several methods have been well documented for alleviating some of these issues, including the use of fundamental TE and TM mode rectangular metallic waveguides, low-loss cylindrical corrugated HE waveguides [30], quasi-optical propagation systems [30], and in-situ generation and detection of the microwaves [31]. Standing waves are particularly problematic in the case of broadband spectroscopies, e.g. time-domain [31] and Fourier transform techniques [32], as well as for frequency sweepable monochromatic sources [33, 34]. In these instances, the optical properties are usually deduced via reflectivity or transmission measurements, requiring a large well-defined (i.e. at) sample surface area ($> \lambda^2$). For cases in which large

samples are not available (note: spans from 3 cm at 10 GHz to 0.3 mm at 1 THz), resonant techniques become necessary, e.g. cavity perturbation [5, 6, 7, 17, 29]. This unfortunately limits measurements to the modes of the cavity. In addition, making absolute measurements of the optical constants of a sample, as a function of frequency, is extremely difficult to achieve using cavity perturbation because of its narrow-band nature [5, 6, 7]. However, the cavity perturbation technique is ideally suited for fixed-frequency, magnetic resonance measurements [29]. Furthermore, as we have recently shown, it is possible to make measurements at many different frequencies by working on higher order modes of the cavity [29]. To date, measurements in enclosed cylindrical copper cavities have been possible at frequencies up to 350 GHz (see Sec. IIIB).

The standard approach for studying angle-dependent effects using the cavity perturbation technique is to use a split-pair magnet and/or goniometers, and is widely used in lower frequency commercial EPR instruments, e.g. X-band, K-band and Q-band [9, 35]. In the case of the split-pair approach, the DC magnetic field is rotated with respect to a static waveguide/cavity assembly. In this paper, we outline a method for in-situ rotation of part of a cylindrical resonator, thus enabling angle-dependent cavity perturbation measurements in ultra-high-field magnets, and two-axis rotation capabilities in standard high-field superconducting split-pair magnets. As we shall outline, the rotation mechanism preserves the cylindrical symmetry of the measurement, thereby ensuring that the electromagnetic coupling to the microwave fields does not change upon rotating the sample. This is particularly important for studies of low-dimensional conductors, where sample rotation alone (as in the case of a goniometer) would lead to unwanted instrumental artifacts associated with incommensurate symmetries of the sample and cavity. The available frequency range in the setup developed at the University of Florida (UF) spans from 8 GHz up to 700 GHz ($0.27\text{--}23\text{ cm}^{-1}$). Experiments are possible in DC magnetic fields of up to 17 tesla, and at temperatures in the range from 0.5–400 kelvin at UF. Furthermore, all experimental probes and techniques developed at UF, including the ones described in this article, are also compatible with the 45 tesla resistive magnets at the National High Magnetic Field Laboratory (NHMFL) in Tallahassee, FL.

We note that a rotating cavity has previously been developed by Schrama et al. [36], at the University of Oxford, also for high-field microwave studies. As we will demonstrate in this article, the cylindrical geometry offers many advantages over the rectangular design implemented by the Oxford group. For example, the waveguides are coupled rigidly to the cylindrical body of the cavity in our design (only the end-plate rotates), whereas the coupling is varied upon rotation in the Oxford version, resulting in effective “blind-spots”, i.e. angles where the microwave fields in the waveguides do not couple to the cavity; in contrast, the cylindrical version

offers full 360° rotation. Furthermore, the rigid design offers greater mechanical stability and, therefore, less microwave leakage from the cavity, resulting in improved signal-to-noise characteristics [29]. The TE_{01n} cylindrical modes also offer the advantage that no AC currents flow between the curved surfaces and the rotating end-plate of the cylindrical resonator. Consequently, the moving part of the cavity does not compromise the exceptionally high quality (Q) factors associated with these modes. Indeed, Q factors for the first few TE_{01n} modes vary from 10,000 to 25,000 (at low temperatures), as opposed to just 500 for the rectangular cavities. This order of magnitude improvement translates into vastly increased sensitivity, enabling e.g., EPR studies of extremely small single crystal samples. Finally, the cylindrical cavity is machined entirely from copper, and held rigidly together entirely by screws. This all-copper construction results in negligible field sensitivity, i.e. the field dependence of the cavity parameters is essentially flat and, most importantly, the cavities do not contain any paramagnetic impurities that could give rise to spurious magnetic resonance signals.

In the next section, the detailed features of the rotating cavity are described, and some example data obtained with the rotating cavity will be shown in the following section.

II. TECHNICAL DESCRIPTION

A. Overview of experimental setup

As a tunable source of millimeter and sub-millimeter-wave radiation, we use a Millimeter-wave Vector Network Analyzer (MVNA), including an External Source Association (ESA) option. The basic MVNA-8-350-1-2 analyzer utilizes pairs of phase-locked sweepable (8–18.5 GHz) YIG sources and multipliers (Schottky diodes), enabling superheterodyne vector (phase sensitive) measurements, with sufficient dynamic range for the measurements described in this paper, to frequencies on the order of 250 GHz. Further details concerning the MVNA are published in refs. [29, 33]. The ESA option additionally permits association with a higher frequency Gunn diode source, providing enhanced signal-to-noise characteristics in the 150–250 GHz range, as well as enabling measurements to considerably higher frequencies (up to 700 GHz, or 23 cm^{-1} [33]). For the purposes of this article, we note that the ESA option can be used very effectively for studies on higher order modes of the rotating cavity (150 up to almost 400 GHz—see section III). A detailed description of the use of the MVNA for cavity perturbation measurements up to 200 GHz, including a description of the waveguide coupling between the MVNA and the low-temperature/high-field environment, has been presented previously by Mola et al. [29]. For measurements above 400 GHz, we employ a quasi-optical bridge coupled to a simple reflectivity probe (with no cavity) constructed

TABLE I: Available magnet systems at the University of Florida (UF) and the NHMFL. The table lists the field geometry and magnet type, the maximum available field B_{max} , the probe length, the available temperature (T) range, and the outer diameter of the cavity probe.

Magnet	B_{max} (T)	Type	length	T (kelvin)	Probe dia.
45 T (NHMFL)	45	Axial hybrid	1.67 m	1.4 – 300	3/4"
33 T (NHMFL)	33	Axial resistive	1.45 m	1.4 – 300	3/4"
25 T (NHMFL)	25	Axial resistive	1.6 m	0.5 – 300 ^a	1"
Oxford Inst. (UF)	17	Axial SC	1.9 m	0.5 – 300 ^a	1" (7/8" ^a)
QDPPMS (UF)	7	Transverse split-coil SC ^b	1.15 m	1.7 – 400	1"

^a 0.5 – 1.4 K with a ³He refrigerator.

^b Allows two-axis rotation in the Quantum Design (QD) PPM S system [38].

from low-loss cylindrical HE mode waveguide; this instrumentation will be described elsewhere [37].

The various magnet systems which are compatible with the instrumentation described in this article are listed in TABLE I. The standard cryostats designed for these magnets are all ⁴He based (either bath or flow cryostats). Because of the demand to work at lower temperatures, we have constructed a simple ³He refrigerator which is compatible with the 17 tesla Oxford Instruments superconducting magnet at UF, and the 25 T resistive magnets at the NHMFL, as listed in TABLE I. A schematic of this refrigerator is shown in Fig. 1. The 1.9 m long waveguide/cavity probe is inserted directly into the ³He space, which is constructed from a 7/8" (= 22.2 mm) outer diameter stainless steel tube with a 0.010" (= 0.25 mm) wall thickness. The lower 254 mm of this tube is double jacketed with a 1.00" (= 25.4 mm) outer diameter. The volume between the two tubes is vacuum sealed in order to provide thermal isolation between the ³He liquid and the surrounding ⁴He vapor. The ³He condenses by means of heat exchange with the walls of the 7/8" tube (above the double jacketed region) which is inserted into the Oxford Instruments ⁴He flow cryostat operating at its base temperature of 1.4 K. After condensation of the full charge of ³He (5 liters at STP), sub-kelvin temperatures are achieved by pumping directly on the liquid by means of an external sealed rotary pump. The refrigerator operates in single-shot mode, i.e. the ³He is returned to a room temperature vessel, where it is stored until the next cooling cycle. A simple gas handling system controls the condensation of ³He gas, and the subsequent pumping of the gas back to the storage vessel. The ³He tube and gas handling system is checked for leaks prior to each cool down from room temperature. Although this design is simple, it has the disadvantage that the microwave probe comes into direct contact with the ³He vapor, thus potentially affecting the tuning of the cavity, as well as the phase of the microwaves reaching the cavity via over 3.8 m of waveguide; such phase fluctuations can cause drifts in signal intensity due to unavoidable standing waves in the waveguide. However, we have found that these problems are minimal when operating at the base

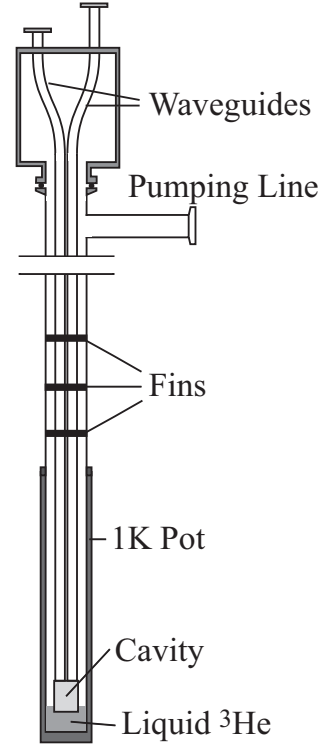


FIG. 1: A schematic diagram of the ³He probe used for sub-kelvin experiments in the Oxford Instruments 17 T superconducting magnet. See main text for a detailed description of its construction.

³He vapor pressure (0.15 torr). The temperature of the sample is then controlled by supplying heat to the copper cavity, which acts as an excellent heat reservoir, i.e. it ensures good thermal stability. The base temperature of the ³He refrigerator is 500 mK and it provides hold times of up to 2 hours.

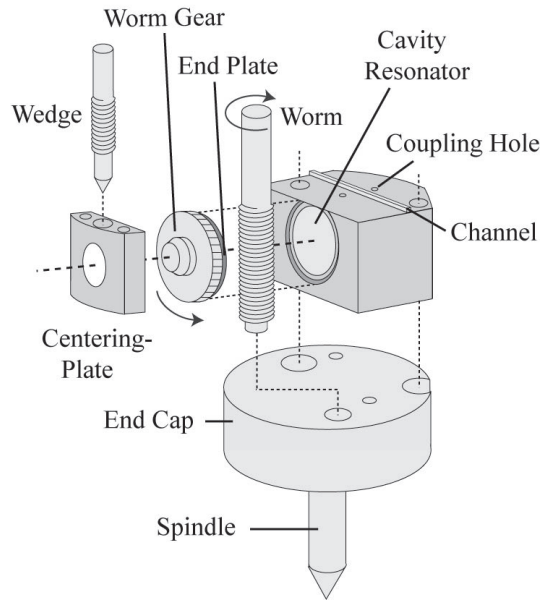


FIG. 2: A schematic diagram of the various components that make up the rotating cavity system. The sample may be placed on the end plate, which can then be rotated via an externally controlled worm drive. The wedge is used to clamp and un-clamp the end plate to/from the main resonator. See main text for a detailed description of the assembly and operation of the rotating cavity.

B. Rotating cavity

The configuration of the rotating cavity is shown in Fig. 2. The principal components consist of the open-ended cylindrical resonator, the cavity end-plate and worm gear, a worm drive for turning the end-plate, and a wedge which facilitates external clamping and un-clamping of the cavity and end-plate. The cavity assembly is mounted on the under-side of a stage (not shown in Fig. 2), and the end-plate is centered on the axis of the cavity by means of a centering-plate. The upper part of the wedge is threaded, and passes through a threaded channel in the stage so that its vertical position can be finely controlled via rotation from above. Likewise, the worm drive is rotated from above, and accurately aligned with the worm gear via an unthreaded channel in the stage. Finally, the worm-drive and centering plate are additionally constrained laterally by means of an end cap and spindle (see below) which attaches to the under side of the resonator. The cavity, end plate, and stage are each machined from copper, thus ensuring excellent thermal stability of the environment surrounding the sample; the heater and thermometry are permanently contacted directly to the stage. The remaining components shown in Fig. 2 are made from brass [39].

The internal diameter of the cavity (7.62 mm) is slightly less than the diameter of the end-plate, which is free to rotate within a small recess machined into the opening of the resonator. On its rear side, the copper

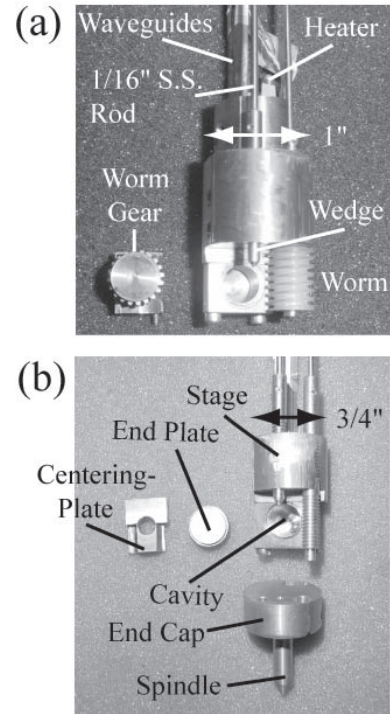


FIG. 3: Photographs of the rotating cavity system; part of the cavity has been disassembled (end-plate and centering-plate) in order to view the inside of the cylindrical resonator. (a) shows the 1st generation rotating cavity, which fits into a 1" thin-walled stainless steel tube; this cavity is compatible with the 25 T magnets at the NHMFL and the QD PPM S and Oxford Instrument magnets at UF (see Table I). (b) shows the 2nd generation rotating cavity, which fits into a 3/4" thin-walled tube; this cavity is compatible with the highest field (45 T) resistive magnets at the NHMFL, as well as the ^3He probe designed for the Oxford Instrument magnet at UF (see Fig. 1).

end-plate mates with a brass gear which, in turn, rotates on an axis which is fixed by the centering-plate. As mentioned above, rotation of the worm gear and end-plate is achieved by turning the worm drive with the wedge disengaged from the end-plate. During experiments, a good reproducible contact between the end-plate and the main body of the cavity is essential for attaining the highest resonance Q -factors. This is achieved by engaging the wedge through a vertical channel in the centering-plate, where it transfers pressure along the axis of the end-plate. Fig. 3 displays labeled photographs of the 1st and 2nd generation rotating cavity assemblies. The 2nd generation version employs a smaller home-built worm drive, reducing the overall diameter of the probe to slightly below 3/4" (≈ 19.1 mm), which enables its use in the highest field magnets at the NHMFL; the 1st generation probe has an outer diameter of just under 1".

The wedge and worm gear are driven by stainless steel rods (diameter = 1/16", or 1.59 mm) which pass through vacuum tight O-ring seals at the top of the waveguide

probe. Small set screws are used to fix the steel control rods into the worm drive and wedge (Fig. 2), and to fix the end-plate within the worm gear. Rotation of the worm gear is monitored via a simple turn-counting dial mounted at the top of the probe, having a readout resolution of 1/100th of a turn. Different worm drive/gear combinations are employed in the 3/4" and 1" diameter probes (see Fig. 3), with 1/41 and 1/20 gear ratios, respectively. Thus, the angle resolution on the dial readout corresponding to the actual sample orientation is approximately 0.09° for the 3/4" probe, and 0.18° for the 1" probe. Although both probes exhibit considerable backlash ($\approx 1^\circ$), this is easily avoided by consistently varying the sample orientation in either a clockwise or counter-clockwise sense. High resolution EPR measurements on single molecule magnets (reported in section III) have confirmed the angle resolution figures stated above.

The stage also performs the task of clamping the V-band waveguides into position directly above the cavity coupling holes. As with previous cavity designs, a small channel [0.02" (= 0.51 mm) wide and 0.02" deep] is machined between the waveguides on the under side of the stage; this channel mates with a similarly sized ridge located in between the coupling holes on the upper surface of the cavity housing (see Fig. 2). Our previous studies have demonstrated that this arrangement is extremely effective at minimizing any direct microwave leak between the incident and transmission waveguides and is, therefore, incorporated into all of our cavity designs [29]. A direct leak signal can be extremely detrimental to cavity perturbation measurements, causing a significant reduction in the useful dynamic range, and to uncontrollable phase and amplitude mixing, as explained in our previous paper [29].

The internal dimensions of the cylindrical resonator are 7.62 mm (diameter) \times 7.62 mm (length). The center frequency of the TE₀₁₁ mode of the unloaded cavity (f_0) is 51.863 GHz, with the possibility to work on higher-order modes as well. Using the ESA option, we have been able to conduct measurements up to 350 GHz [37]. While the modes above about 150 GHz are not well characterized, they do provide many of the advantages of the well-defined lower frequency modes, e.g. enhanced sensitivity, control over the electromagnetic environment (i.e. E vs. H field) at the location of the sample, and some immunity to standing waves. Table II shows resonance parameters for several unloaded cavity modes (there are many others which are not listed). The TE_{01n} (n = positive integer) modes are probably the most important for the rotating cavity design, because their symmetry is axial. Thus, rotation of the end-plate not only preserves the cylindrical symmetry, but also ensures that the sample remains in exactly the same electromagnetic environment, i.e. upon rotation, the polarization remains in a fixed geometry relative to the crystal. A sample is typically placed in one of two positions within the cavity: i) directly on the end-plate; and ii) suspended along the axis of the cavity by means of a quartz pillar

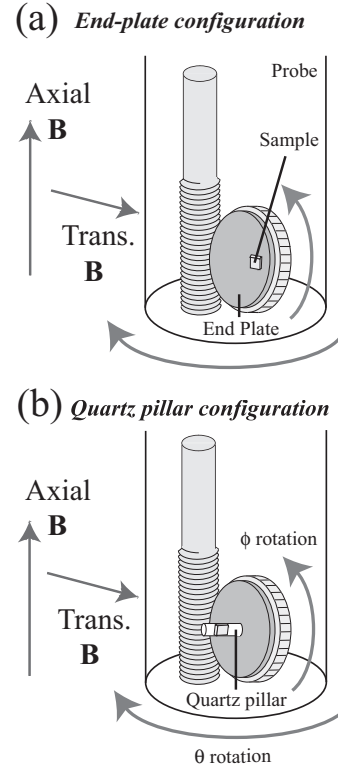


FIG. 4: Schematic diagrams showing various different sample mounting configurations for both axial and transverse magnetic field geometries, including the two-axis rotation capabilities.

(diameter = 0.75 mm) which is mounted in a small hole drilled into the center of the end-plate. These geometries are depicted in Fig. 4 for the TE₀₁₁ mode, and for the two DC magnetic field geometries, i.e. axial and transverse. Each geometry possesses certain advantages for a particular type of experiment. For example, the quartz pillar configuration is particularly useful for EPR experiments in the axial high-field magnets [Fig. 4 (b)] since, for the TE_{01n} modes, the sample sits in a microwave AC field (H_1) which is always transverse to the DC magnetic field (B_0). We discuss this in more detail in section III, and in ref. [29].

Another advantage of the TE_{01n} modes is the fact that no microwave currents flow between the end-plate and the main body of the resonator. Thus, the Q -factors of these modes are high, and essentially insensitive to the mechanical contact made with the wedge. Table II lists the key resonance parameters associated with several modes. For the case of the TE₀₁₁ mode, the low-temperature (2 K) Q -factor is 21,600, and the contrast between the amplitude on resonance [$A(f_0)$] and the amplitude far from resonance (leak amplitude, A_L) is 31.7 dB. These parameters are essentially the same as the optimum values reported for the fixed cylindrical geometry in our earlier paper [29], thus confirming the suitability of this new rotating design for cavity perturba-

TABLE II: Resonance parameters for several different cavity modes. The first column indicates the given mode. The second column lists the resonance frequencies (f_0). The third column lists the Q -factors. The final column lists the contrast in dB, i.e. $A(f_0) - A_1$, where $A(f)$ is the transmission amplitude at the resonance frequency, f , and A_1 is the leak amplitude.

Mode	f_0 (GHz)	Q	$A(f_0) - A_1$ (dB)
TE011	51.863	21,600	31.7
TE212	54.774	3,300	26.5
TE012	62.030	16,600	25.2
TE015	109.035	8,600	19.0

tion studies of small single-crystal samples, both insulating and conducting. We note that the Q -value for the non-cylindrically symmetric mode in Table II (TE212) is almost an order of magnitude lower than that of the TE011 mode. As noted above, this is due to the flow of microwave currents associated with the TE212 mode across the mechanical connection between the main body of the resonator and the end-plate.

As discussed earlier, even though the end-plate can be rotated, the waveguides are coupled absolutely rigidly to the cavity via the stage. As with earlier designs [29], the microwave fields in the waveguides are coupled into the resonator by means of small circular coupling holes which are drilled through the sidewalls of the cavity. The sizes of these coupling holes [diameter = 0.038" (≈ 0.97 mm), or ≈ 6] have been optimized for the V-band, and the cavity side-wall was milled down to a thickness of 0.015" (≈ 0.38 mm, or ≈ 15) at the location of these holes. Once again, these numbers are essentially the same as those reported in ref. [29]. The key point here is that this coupling never changes during rotation. Therefore, the full 360° angle range may be explored, and with excellent mechanical stability. Fig. 5 shows the typical random fluctuations in the cavity resonance parameters for the TE01n mode during a complete 360° rotation of the end-plate: the center frequency varies by no more than

120 kHz (≈ 3 ppm, or 5% of the resonance width); the Q -factor is essentially constant, to within 1%; and the contrast, $[A(f_0) - A_1]$, fluctuates between 29 dB to 33 dB, corresponding respectively to leak amplitudes of 3.5% and 2.2% of $A(f_0)$. Another important consequence of coupling through the side walls of the cavity involves selection rules for TM cylindrical cavity modes. At the lowest frequencies, only the TE01 mode of the V-band waveguide propagates. Thus, the microwave H_1 field in the waveguide is polarized parallel to the cavity axis, i.e. it is incompatible with the symmetry associated with the H_1 patterns of the TM modes. Consequently, we do not observe, for example, the TM111 mode. This offers added benefit, since the TM11n modes are ordinarily degenerate with the TE01n modes, and steps have to be taken to either lift these degeneracies, or to suppress the TM modes all together [29]. Here, we simply do not

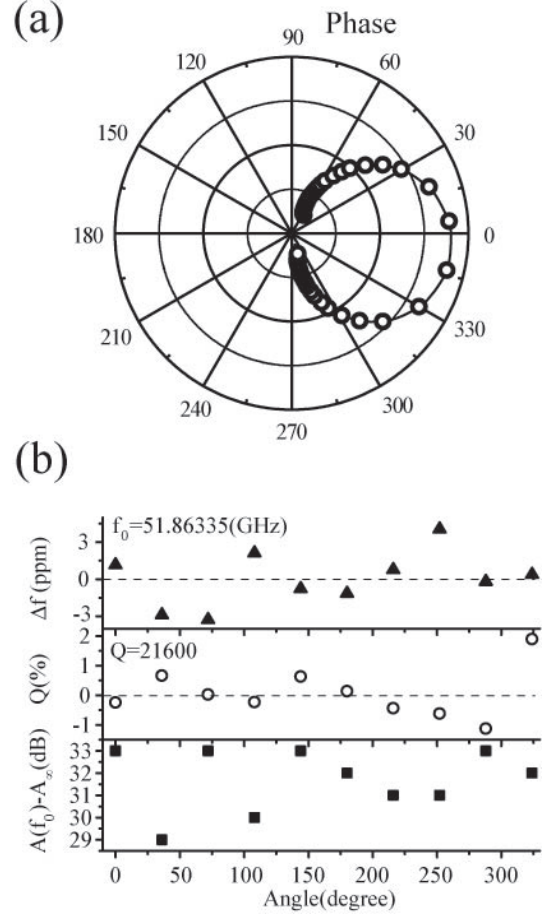


FIG. 5: (a) A polar plot of the complex signal transmitted through the cavity as the frequency is swept through the TE011 mode; the polar coordinate represents the phase of the transmitted signal, while the radial coordinate corresponds to the linear amplitude. The Lorentzian resonance is observed as a circle in the complex plane. Points close to the origin correspond to frequencies far from resonance, while the resonance frequency corresponds to the point on the circle furthest from the origin. The resonance parameters are obtained from fits (solid line) to the data (open circles) in the complex plane (see ref. [29] for a detailed explanation of this procedure). The average center frequency, f_0 , is 51.863 GHz, and the Q factor is 21600. (b) Full 360° angle-dependence of the fluctuations in the resonance parameters for the TE011 mode: upper panel f_0 ; center panel Q ; and lower panel difference between the amplitude on resonance $[A(f_0)]$ and the amplitude far from resonance (the leak amplitude, A_1). These data illustrate the excellent reproducibility of the resonance parameters upon un-clamping, rotating, and re-clamping the cavity.

couple to these modes at the lowest frequencies. Even at the highest frequencies, we do not expect coupling to TM modes, provided the polarization of the microwave sources is maintained throughout the waveguide.

The main design challenge in the development of a useful rotating cavity system concerned the space constraints imposed by the high-field magnets at the

NHMF; the specifications of each magnet system are listed in Table I. A prototype configuration was first developed, based on a 1" outer tube diameter. This prototype was subsequently implemented in both magnet systems at UF, and in the 25 T, 50 mm bore resistive magnets at the NHMF. A picture of this cavity system, which remains in use, is shown in Fig. 3(a). The major reason for the large size of the cavity assembly is the large worm drive diameter ($3/8" = 9.525 \text{ mm}$), which is determined by the smallest readily available commercial components [40]; this 1st generation worm drive is made of nylon. A more compact 2nd generation rotating cavity was developed by machining a considerably smaller custom worm drive (and gear) in-house. This cavity assembly, which is shown in Fig. 3(b), is small enough to fit into a $3/4"$ diameter thin-walled stainless steel tube, thus enabling measurements in the highest field 45 T hybrid magnet at the NHMF. Furthermore, this cavity is compatible with the ^3He probe constructed for the 17 T Oxford Instruments superconducting magnet (and the 25 T resistive magnet at the NHMF), allowing for experiments at temperatures down to 500 mK. We note that the 1st and 2nd generation cavity assemblies may be transferred relatively easily from one particular waveguide probe to another, requiring only that the thermometry be unglued and re-glued to the stage using GE varnish; all other connections are made with screws. In addition, we have constructed extra parts for both designs, including several cavities and end-plates. This enables preparation of a new experiment while an existing experiment is in progress.

Finally, we discuss the two-axis rotation capabilities made available via a 7 T Quantum Design (QD) magnet (see Table I). The 7 T transverse QD system is outfitted with a rotation stage at the neck of the dewar. A collar clamped around the top of the waveguide probe mounts onto this rotation stage when the probe is inserted into the PPM slow-cryostat [38]. The rotator is driven by a computer controlled stepper motor, with 0.01° angle resolution. The motor control has the advantage that it can be automated and, therefore, programmed to perform measurements at many angles over an extended period of time without supervision. In the 50–250 GHz range, the compact Schottky diodes can be used for microwave generation and detection. These devices are mounted directly to the probe, and are linked to the MVNA via flexible coaxial cables (feeding the diodes with a signal in the 8–18 GHz range). Therefore, the waveguide probe can rotate with the source and detector rigidly connected, while the vacuum integrity of the slow cryostat is maintained via two sliding O-ring seals at the top of the dewar. In fact, this arrangement rotates so smoothly that it is possible to perform fixed-field cavity perturbation measurements as a function of the field orientation, as has recently been demonstrated for the organic conductor $-(\text{BEDT-TTF})_2\text{KHg}(\text{SCN})_4$ [15]. We generally use the stepper motor to control the polar coordinate, while mechanical control of the cavity end-plate is used to vary

the plane of rotation, i.e. the azimuthal coordinate.

Due to the extremely precise control over both angles, and because of the need for such precision in recent experiments on single-molecule magnets which exhibit remarkable sensitivity to the field orientation [41], we have found it necessary to make two modifications to the $3/4"$ rotating cavity probe for the purposes of two-axis rotation experiments. The first involves constraining the cavity assembly and the waveguides within a $3/4"$ thin-walled stainless steel tube which is rigidly connected to the top of the probe. This tube reduces any possible effects caused by magnetic torque about the probe axis, which could mis-align the cavity relative to the rotator. The second modification involves attaching a spindle on the under-side of the end-cap. This spindle locates into a centering ring attached to the bottom of the PPM slow-cryostat, thus preventing the waveguide probe from rotating off-axis (note that the inner diameter of the cryostat is 1.10" as opposed to the $3/4"$ outer diameter of the probe).

III. EXPERIMENTAL TESTS

In this section, we present two examples of unique experiments which were recently performed using the rotating cavity. We also assess the performance of the instrument.

A. High-field angle-dependent cyclotron resonance in $-(\text{ET})_2\text{Cu}(\text{NCS})_2$

One of the greatest benefits of the rotating cavity is the possibility to perform angle-dependent electrodynamic studies in the high-field magnets at the NHMF. Microwave absorption in a magnetic field can be used to gain important information about the Fermi surfaces and other fingerprints associated with the itinerant electrons in many materials of current fundamental and technological interest, particularly low-dimensional conductors and superconductors. These measurements typically require the ability to orient the magnetic field relative to a single-crystal sample. This can easily be achieved at low fields by rotating a horizontal field magnet, changing the currents in orthogonal Helmholtz magnet pairs, or by rotating the entire measurement apparatus in a split solenoid with radial access. However, these approaches are currently limited by the available magnets to fields below about 10 T. While relatively high-field split-pair magnets are planned in the future at the NHMF, these will still be limited to roughly 20 T, since the split dramatically reduces the attainable field. Thus, an in-situ sample rotation capability is essential for very high-field studies. In this section, we highlight these capabilities using as an example the observation of a novel form of quasi-one-dimensional (Q1D) cyclotron resonance (CR) in a low-dimensional organic conductor [15].

The organic charge-transfer-salts (CTSs) $-(\text{ET})_2\text{X}$ (anion: $\text{X} = \text{Cu}(\text{NCS})_2$, I_3 , $\text{CuN}(\text{CN})_2\text{Br}$, etc.) are quasi-two-dimensional (Q2D) conductors consisting of layers of stacked bis-(ethylenedithio)-tetrathiafulvalene (BEDT-TTF or ET for short), separated by insulating anion layers. The separation between the conducting layers is sufficient to treat the ET CTSs as Q2D systems. At low temperatures, the $-(\text{ET})_2\text{X}$ CTSs become superconducting, with many properties similar to the high-temperature cuprate superconductors, e.g.: an anisotropic superconducting state [42], with the possibility of a nodal energy gap [43]; a phase diagram which consists of an antiferromagnetic insulating phase in close proximity to a superconducting phase; and an unconventional metallic phase [44]. The FS of the $\text{X} = \text{Cu}(\text{NCS})_2$ CTS, as calculated using an extended tight binding model [45], consists of a pair of corrugated Q1D (open) electron sheets and a closed Q2D hole pocket. When a magnetic field is applied in the plane of the Q1D FS, charged particles move in response to the Lorentz force along periodic momentum-space trajectories across the Q1D FS sheets. During this motion, the Fermi velocity, v_F , remains exactly perpendicular to the FS. Consequently v_F becomes oscillatory due to the periodic corrugation of the FS. This oscillatory velocity results in a conductivity resonance the so-called periodic-orbit-resonance (POR [11, 15]). This Q1D POR can be distinguished from the usual CR by its angle dependence [15], which is given by,

$$\frac{\omega}{B_{jj}} = \frac{ev_F R_{jj}}{h} \sin(\theta) \quad (1)$$

where ω is the microwave frequency, B_{jj} is the projection of the magnetic field (B) onto the plane of the FS, R_{jj} is the projection of the lattice vector associated with the FS corrugation onto the FS, and θ is the angle between the corrugating axis (along \hat{a}) and B_{jj} ; e is the electron charge, and h is the Planck constant. One can, therefore, determine v_F and the direction of the corrugation axis, \hat{a} , by studying angle dependent Q1D POR.

Measurements for $\text{X} = \text{Cu}(\text{NCS})_2$ were carried out using the 33 tesla resistive magnet at the NHMFL. The high fields are needed in order to access the metallic phase at low temperatures (~ 1.5 K), since the superconducting critical field $B_{c2}^?$ is ~ 5 T for fields perpendicular to the layers and $B_{c2}^k \sim 30$ T for fields parallel to the layers. The flat platelet-shaped sample was mounted on a quartz pillar, attached to the cavity end-plate [Fig. 4(b)], enabling field rotations in a plane perpendicular to the highly conducting b-c plane (k to the platelet). Experimental spectra obtained at different angles are shown in Fig. 6(a). The data contain extremely rich information, including: a Q1D POR, as indicated by the dashed line; Shubnikov-de Haas (SdH) oscillations at high-fields; and a Josephson plasma resonances (JPR) associated

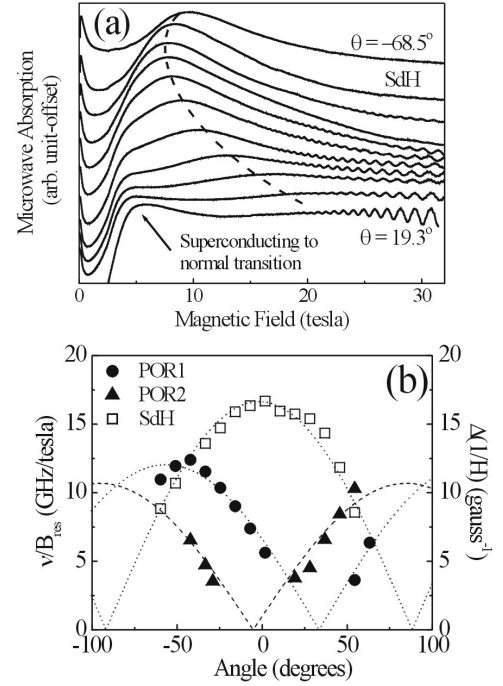


FIG. 6: (a) 1.4 K experimental traces of the 95 GHz microwave absorption, as a function of the magnetic field strength, for different field orientations; θ represents the angle between the least conducting direction (\hat{a} to the b-c plane) and the applied field, and the angle step is 8.78° . The broad absorption peak, which moves to higher fields upon rotating from 68.5° towards 0° (indicated by the dashed curve), corresponds to the Q1D POR. The relatively angle-independent peak at low fields corresponds to a Josephson plasma resonance associated with the superconducting state [25]. At high fields, SdH oscillations are observed. These may be used to locate the least conducting direction. (b) A summary of the angle dependence of two observed series of Q1D POR [only 1 series is shown in (a)], and of the frequency of the SdH oscillations. The dashed curves are theoretical fits to the data. In the case of the Q1D POR, the fits are used to determine the orientations of the Q1D FS corrugation axes, and the Fermi velocity [15, 47].

with the superconducting to normal conducting transition at low fields [25]. The angle dependence of the POR position [Fig. 6(a)], and the SdH oscillation frequency, are plotted in Fig. 6(b). The SdH oscillations are governed by the closed trajectories on the hole FS; thus, their angle-dependence should be the same as that for a Q2D CR [46]. However, the angle dependence of the observed POR in Fig. 6 is clearly quite different from the SdH oscillations. Furthermore, the behavior depends on the plane of rotation (not shown, see ref. [47]). Therefore, this implies that the POR originates from the Q1D FS. Fitting of the two observed POR series [Fig. 6(b)] to Eq. 1 allows us to determine the orientations of the corrugation axes at $\theta = 19.7 \pm 0.5^\circ$ and $34.7 \pm 1.5^\circ$ away from the crystallographic a axis. These directions

correspond to the T_{10} and T_{11} directions, where T_{mn} is related to the primitive lattice vectors, $T_{mn} = ma + nc$. We also obtained a value for the Fermi velocity, $v_F = 3.3 \times 10^6$ m/s.

B. Angle-dependent high-frequency EPR studies of single-molecule magnets

Our more recent research efforts have focused on nanometer scale single-molecule magnets (SMMs) consisting of a core of strongly exchange-coupled transition metal ions (e.g. Mn, Fe, Ni or Co) that collectively possess a large magnetic moment per molecule, thus far up to approximately $51 \mu_B$ ($S = 51/2$) [48]. SMMs offer a number of advantages over other types of magnetic nanostructures. Most importantly, they are monodisperse: each molecule in the crystal has the same spin, orientation, magnetic anisotropy and molecular structure [49]. They thus enable fundamental studies of properties intrinsic to magnetic nanostructures that have previously been inaccessible. For example, recent studies of SMMs have revealed the quantum nature of the spin-dynamics in a nanomagnet: a metastable state of the magnetization, say "spin-up," has been convincingly shown to decay by quantum tunneling through a magnetic anisotropy barrier to a "spin-down" state, in a process called quantum magnetization tunneling (QMT) [49, 50, 51]. Remarkably, QMT in SMMs can be switched on and off, either via a small externally applied field, or by chemically controlling local exchange interactions between pairs (dimers) of SMMs, so-called "exchange-bias" [19]. Thus, the prospects for quantum control and quantum information processing are very exciting.

All known SMMs possess a dominant uniaxial magnetic-crystalline anisotropy and, to lowest order, their effective spin Hamiltonian may be written

$$\hat{H} = D \hat{S}_z^2 + g_B \vec{B} \cdot \hat{\vec{S}} + \hat{H}^0; \quad (2)$$

where D (< 0) is the uniaxial anisotropy constant, the second term represents the Zeeman interaction with an applied field \vec{B} , and \hat{H}^0 includes higher order terms in the crystal field, as well as environmental couplings such as intermolecular interactions [18, 20, 49]. This Ising-type anisotropy is responsible for the energy barrier to magnetization reversal and the resulting magnetic bistability-factors which lead to magnetic hysteresis at sufficiently low temperatures. QMT in zero-field is caused by interactions which lower the symmetry of the molecule from strictly axial, thereby mixing otherwise degenerate pure "spin-up" and "spin-down" states. QMT rates depend on the degree of symmetry breaking, which can be determined very precisely via angle-dependent single-crystal EPR measurements.

The first SMM, $\text{Mn}_{12}\text{O}_{12}(\text{CH}_3\text{COO})_{16}(\text{H}_2\text{O})_4 \cdot 2\text{CH}_3\text{COOH} \cdot 4\text{H}_2\text{O}$ ($\text{Mn}_{12}\text{-Ac}$), has become the most widely

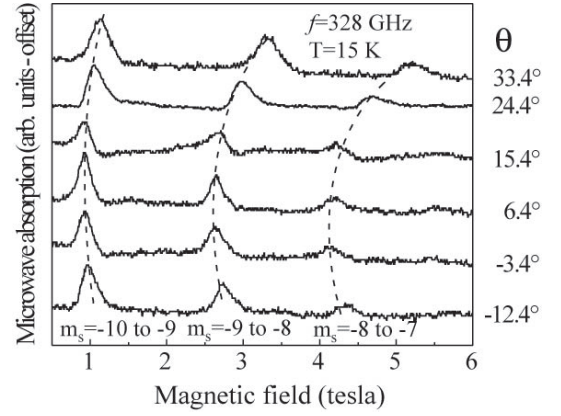


FIG. 7: The angle dependence of the high-frequency EPR spectrum obtained for the $\text{Mn}_{12}\text{-Ac}$ single-molecule magnet [55]; $\theta = 0$ corresponds to the field applied exactly parallel to the easy-axis of the crystal. The peaks are labeled according to the m_s levels involved in the transitions.

studied, due to its giant spin ($S = 10$) ground state and its high symmetry (S_4) [49, 52]. These factors result in the largest known blocking temperature ($T_B \approx 3$ K) against magnetization relaxation of any SMM. In spite of over 10 years of research, a clear picture has only recently emerged concerning the symmetry breaking responsible for the QMT in $\text{Mn}_{12}\text{-Ac}$ [20, 53, 54]. Several studies have shown that disorder associated with the acetic acid solvent in $\text{Mn}_{12}\text{-Ac}$ leads to discrete local environments, resulting in a significant fraction of the molecules ($> 50\%$) possessing two-fold symmetry, with a rhombic crystal-field term E of order 0.01 cm^{-1} (or $E/D \approx 0.02$) [20].

In Fig. 7, we show very high frequency EPR spectra obtained for several field orientations close to the easy-axis of a single-crystal sample (volume 0.2 mm^3) [55]; the temperature is 15 K and the frequency is 328 GHz, corresponding to a very high-order mode of the cavity. The peaks in the transmission through the cavity correspond to EPR, and the resonances have been labeled in the figure according to the m_s levels involved in the transitions. In spite of the high frequency, the signal-to-noise is good, and the resonances are relatively symmetric, indicating minimal phase and amplitude mixing. Indeed, the data are comparable in quality with previously published data at much lower frequencies ($< 200 \text{ GHz}$) [56]. These experiments were performed using the ESA extension (Gunn diode) with the MVNA, and the sample was mounted on the end-plate. Although the electromagnetic field distribution at the location of the sample is not known for such a high-order mode of the cavity, it can be assumed that there is a significant H_1 component transverse to the applied DC field. Due to the significant axial crystal-field splitting in $\text{Mn}_{12}\text{-Ac}$ (Eq. 2), the ground state ($m_s = -10$) to first excited state ($m_s = -9$) separation is on the order of 300 GHz in zero field. Therefore, the $m_s = -10 \rightarrow -9$ transition is inaccessible below

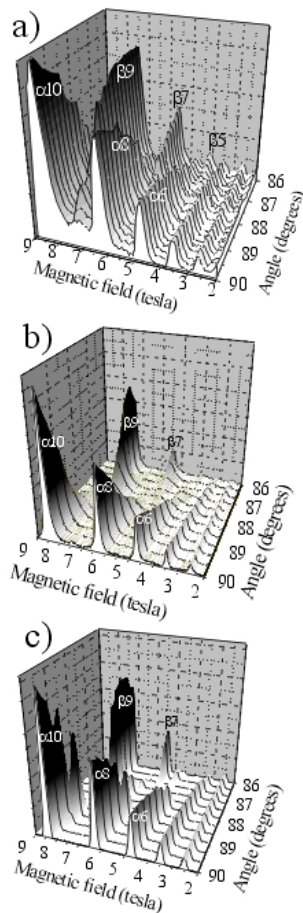


FIG. 8: 3D grey-scale plots of the angle dependence of the low-frequency (51.5 GHz, 15 K) hard-plane EPR spectra obtained for (a) $Mn_{12}\text{-Ac}$ [41] and (b) $Mn_{12}\text{-BrAc}$ [57]; $\theta = 90^\circ$ corresponds to the field applied exactly parallel to the hard-plane of the crystal. Simulated spectra (51.5 GHz, 15 K) are displayed for comparison in (c); the simulations were generated using accepted Hamiltonian parameters, which are essentially identical for the two complexes [41]. See main text and refs. [41, 57] for an explanation of the data.

300 GHz; hence the requirement for high frequencies. At low fields, the positions of the EPR peaks are affected mainly by the field component parallel to the easy axis of the crystal ($\propto \cos \theta$, where θ is the angle between the applied field and the easy axis), as observed in Fig. 7. Thus, two-axis rotation experiments may be used to locate the easy axis.

In Fig. 8, we compare high-resolution angle-dependent high-field EPR spectra at 51.5 GHz and 15 K, for field orientations close to the hard plane ($\theta \approx 90^\circ$), obtained for two forms of Mn_{12} : (a) the standard $Mn_{12}\text{-Ac}$; and (b) another high-symmetry (S_4)

complex, $[Mn_{12}O_{12}(O_2CCH_2Br)_{16}(H_2O)_4] \cdot 4CHCl_2$, or $Mn_{12}\text{-BrAc}$ [57]. Both data sets were collected in an axial high-field magnet, with the needle-shaped samples mounted directly on the end-plate of the cavity such that $H_1 \parallel B$, as illustrated in Fig. 4a. The two Mn_{12} complexes differ only in their ligand and solvent molecules, otherwise the $Mn_{12}O_{12}$ cores are identical. Indeed, the average crystal-field parameters for the two complexes are essentially the same [41, 57]. However, the spectra for $Mn_{12}\text{-Ac}$ exhibit considerable complexity in comparison to $Mn_{12}\text{-BrAc}$, e.g. the EPR peaks are broader, asymmetric, and contain several fine structures (see ref. [41] for more details). Perhaps the most striking difference in the spectra for the two complexes is the significant overlap of the α_8 and α_9 series of resonances for the $Mn_{12}\text{-Ac}$ sample. The origin of the α_8 and α_9 resonances is discussed in detail in ref. [41], and is beyond the scope of this article. Nevertheless, simulated spectra (also for 51 GHz and 15 K) are displayed in Fig. 8c, which indicate that the α_{10} and α_8 peaks should not overlap in angle with the α_9 resonance. In this respect, the data for the $Mn_{12}\text{-BrAc}$ complex exhibit good agreement with the simulations. In contrast, the overlapping of the α_8 and α_9 resonances have provided the first indications that the molecular easy axes for the $Mn_{12}\text{-Ac}$ complex are tilted locally (up to 1:7 [41]). Such tilting can be understood within the context of the solvent disorder picture [53]: the various fine structures, and angular overlap of different portions of the EPR spectra, reflect a (discrete) distribution of local environments caused by the solvent disorder. Using the two axis rotation capabilities, more recent studies have confirmed the discrete nature of the local environments, e.g. the molecular easy axis tilts are confined to orthogonal planes, and each of the EPR fine structures has its own distinct angle dependence [58]. Meanwhile, none of the fine-structures are seen in the $Mn_{12}\text{-BrAc}$ complex, thus confirming the idea that the acetic acid solvent significantly influences the magnetization dynamics in $Mn_{12}\text{-Ac}$. Indeed, the EPR spectra for $Mn_{12}\text{-BrAc}$ provide unprecedented resolution, allowing for unique spectroscopic insights into high-symmetry giant spin SMMs [57].

Acknowledgments

The authors appreciate useful discussions with Rachel Edwards, Alexey Kovalev and Bruce Brandt. We would also like to thank Daniel Benjamin, Marc Link, Mike Herlevich and John Van Leer for technical assistance. This work was supported by the National Science Foundation (DMR 0196461 and DMR 0239481), and by Research Corporation. Work at the NMMFL is supported by a cooperative agreement between the State of Florida and the National Science Foundation through NSF-DMR-0084173.

-
- [1] D.M. Littleman, R.H. Jacobsen, and M.C. Nuss, *IEEE J. Sel. Top. Quantum Electron.* 2, 679 (1996).
- [2] D.M. Littleman, M. Gupta, R. Neelamani, R.G. Baraniuk, J.V. Rudd, and M. Koch, *Appl. Phys. B* 68, 1085 (1999).
- [3] M. Hermann, M. Tani, K. Sakai, and R. Fukasawa, *J. Appl. Phys.* 91, 1247 (2002).
- [4] P.Y. Han, G.C. Cho, and X.C. Zhang, *Opt. Lett.* 25, 242 (2000).
- [5] O. Klein, S. Donovan, M. Dressel, and G. Gruner, *Int. J. Infrared and Millimeter Waves* 14, 2423 (1993).
- [6] S. Donovan, O. Klein, M. Dressel, K. Holczer, and G. Gruner, *Int. J. Infrared and Millimeter Waves* 14, 2459 (1993).
- [7] M. Dressel, O. Klein, S. Donovan, and G. Gruner, *Int. J. Infrared and Millimeter Waves* 14, 2489 (1993).
- [8] D.A. Bonn and W.N. Hardy, in *Physical Properties of High Temperature Superconductors V*, Chapter 2 (World Scientific Publishing Company, 1996).
- [9] A.F. Kip, D.N. Langenberg, and T.W. Moore, *Phys. Rev.* 2, 359 (1961).
- [10] T.W. Moore and F.W. Spong, *Phys. Rev.* 3, 846 (1962).
- [11] S. Hill, *Phys. Rev. B* 55, 4931 (1997).
- [12] S.J. Blundell, A. Ardavan, and J. Singleton, *Phys. Rev. B* 55, R6129 (1997).
- [13] A. Ardavan, J.M. Schram, S.J. Blundell, J. Singleton, W. Hayes, M. Kumoo, and P. Day, *Phys. Rev. Lett.* 81, 713 (1998).
- [14] S. Hill, J.S. Brooks, Z.Q. Mao, and Y. Maeno, *Phys. Rev. Lett.* 84, 3374 (2000).
- [15] A.E. Kovalev, S. Hill, and J. Qualls, *Phys. Rev. B* 66, 134513 (2002).
- [16] A.E. Kovalev, S. Hill, K. Kawano, M. Tamura, T. Naito, and H. Kobayashi, *Phys. Rev. Lett.* 91, 216402 (2003).
- [17] C.P. Poole, in *Electron Spin Resonance* (Interscience Publishers, New York, 1967).
- [18] S. Hill, J.A. J. Perenboom, N.S. Dalal, T. Hathaway, and T. Stalcup, *Phys. Rev. Lett.* 80, 2453 (1998).
- [19] S. Hill, R.S. Edwards, N. Aliaga-Alcalde, and G. Christou, *Science* 302, 1015 (2003).
- [20] S. Hill, R.S. Edwards, S.I. Jones, N.S. Dalal, and J.M. North, *Phys. Rev. Lett.* 90, 217204 (2003).
- [21] C. Kittel, in *Introduction to Solid State Physics* (John Wiley and sons, New York, 1976).
- [22] Y. Matsuda, M.B. Gaifullin, K. Kadowaki, K. Kadowaki, and T. Mochiku, *Phys. Rev. Lett.* 75, 4512 (1995).
- [23] M.B. Gaifullin, Y. Matsuda, K. Kadowaki, T. Mochiku, and K. Kumagai, *Physica C* 282-287, 2429 (1997).
- [24] M. Mola, J.T. King, C.P. McRaven, S. Hill, J.S. Qualls, and J.S. Brooks, *Phys. Rev. B* 62, 5965 (2000).
- [25] S. Hill, M. Mola, and J.S. Qualls, *J. Phys. Condens. Matter* 14, 6701 (2002).
- [26] L.W. Engel, D. Shahar, C. Kurdak, and D.C. Tsui, *Phys. Rev. Lett.* 71, 2638 (1993).
- [27] C.C. Li, L.W. Engel, D. Shahar, D.C. Tsui, and M. Shayagan, *Phys. Rev. Lett.* 79, 1353 (1997).
- [28] For example, specifications of the magnets at the NHMFL can be found on-line at www.magnet.fsu.edu/users/facilities/dc_eld.
- [29] M. Mola, S. Hill, P. Goy, and M. Gross, *Rev. Sci. Instrum.* 71, 186 (2000).
- [30] G.M. Smith, J.C.G. Lesurf, R.H. Mitchell, and P.C. Riedi, *Rev. Sci. Instrum.* 69, 3924 (1998).
- [31] A. Nahata, A.S. Weling, and T.F. Heinz, *Appl. Phys. Lett.* 69, 2321 (1996).
- [32] H.M. Heise, E.H. Korte, and H. Siesler, eds., *Proc. 8th Intl. Conf. on Fourier Transform Spectroscopy*, vol. 1575 (SPIE, 1992).
- [33] P. Goy and M. Gross, *Proc. SPIE* 3465, 288 (1998), and detailed information may also be found online at www.abmillimetre.com.
- [34] G. Kozlov and A. Volkov, in *Millimeter and Submillimeter Spectroscopy of Solids*, edited by G. Gruner (Springer Verlag, Berlin Heidelberg, 1998), vol. 74 of *Topics in Applied Physics*.
- [35] W.R. Datars and R.N. Dexter, *Phys. Rev.* 124, 75 (1961).
- [36] J.M. Schram, J. Singleton, R.S. Edwards, A. Ardavan, E. Rzepniewski, R. Harris, P. Goy, M. Gross, J. Schlieter, M. Kumoo, et al., *J. Phys.* 13, 2235 (2001).
- [37] R. Edwards, S. Hill, P. Goy, R. Wylde, and S. Takahashi, *Physica B* 346-347, 211 (2004).
- [38] PPM S Physical Property Measurement System.
- [39] The larger worm gear used in the 1st generation cavities was commercially manufactured from steel.
- [40] Purchased from SDP/SI, www.sdp-si.com.
- [41] S. Takahashi, R.S. Edwards, J.M. North, S. Hill, and N.S. Dalal (2004), in press.
- [42] M. Dressel, O. Klein, G. Gruner, K.D. Carlson, H.H. Wang, and J.M. Williams, *Phys. Rev. B* 50, 13603 (1994).
- [43] K. Izawa, H. Yamaguchi, T. Sasaki, and Y. Matsuda, *Phys. Rev. Lett.* 88, 027002 (2001).
- [44] R.H. McKenzie, *Science* 278, 820 (1997).
- [45] T. Ishiguro, K. Yamaji, and G. Saito, in *Organic Superconductor* (Springer, Heidelberg Germany, 1998).
- [46] D. Shoenberg, in *Magnetic oscillations in metals* (Cambridge University Press, Cambridge, 1984).
- [47] S. Takahashi, A.E. Kovalev, S. Hill, S. Takasaki, J. Yamada, H. Anzai, J.S. Qualls, K. Kawano, M. Tamura, T. Naito, et al. (2004), submitted to *Int. J. Mod. Phys. B*.
- [48] M. Munugesu, M. Habrych, W. Wemtsdorfer, K.A. Abboud, and G. Christou, *J. Am. Chem. Soc.* 126, 4766 (2004).
- [49] D. Gatteschi and R. Sessoli, *Angew. Chem.* 42, 268 (2003).
- [50] J.R. Friedman, M.P. Sarachik, J. Tejada, and R. Ziolo, *Phys. Rev. Lett.* 76, 3830 (1996).
- [51] L. Thomas, F. Linti, R. Ballou, D. Gatteschi, R. Sessoli, and B. Barbara, *Nature* 383, 145 (1996).
- [52] T. Lis, *Acta Crystallogr. B* 36, 2042 (1980).
- [53] A. Comia, R. Sessoli, L. Sorace, D. Gatteschi, A.L. Barra, and C. D'Aiguebonne, *Phys. Rev. Lett.* 89, 257201 (2002).
- [54] E. delBarco, A.D. Kent, E.M. Rumberger, D.N. Hendrickson, and G. Christou, *Phys. Rev. Lett.* 91, 047203 (2003).
- [55] S. Takahashi, S. Hill, J.M. North, and N.S. Dalal (2003), unpublished.
- [56] S. Hill, S. Macagnano, K. Park, R.M. Achey, J.M. North, and N.S. Dalal, *Phys. Rev. B* 65, 224410 (2002).

- [57] K . Petukhov, S . Hill, N . E . Chakov, K . Abboud, and G . Christou, Phys.Rev.B (2004), in press.
- [58] S . Hill, N . Chakov, and G . Christou (2004), unpublished.